Modeling of mechanical behavior in additive manufacturing at part scale Modeling of mechanical behavior in additive manufacturing at part scale

Qiang Chen, Erwan Beauchesne, Francis Arnaudeau, Pierre-Richard Dahoo, Constantin Meis

Modeling of mechanical behavior in additive manufacturing at part scale

Journal of Physics: Conference Series **1391** (2019) 012010 doi:10.1088/1742-6596/1391/1/012010

Modeling of mechanical behavior in additive manufacturing at part scale

Qiang Chen[1], Erwan Beauchesne[2], Francis Arnaudeau[2], Pierre-Richard Dahoo[1] and Constantin Meis[3]

[1] LATMOS, UVSQ/Université Paris-Saclay, 11 Boulevard d4Alembert, 78280 Guyancourt, France
[2] Altair Engineering, 5-10 Rue de la Renaissance, 92160 Antony, France
[3] National Institute for Nuclear Science and Technology, CEA Scalay, 91191 Gif-sur Yvette, France

E-mail: qiang.chen@latmos.ipsl.fr, ebeauche@altair.com, francis@altair.com, pierre.dahoo@uvsq.fr, constantin.meis@cea.fr

Abstract. Laser Beam Melting is actually capable of producing parts with reliable mechanical properties. However, efficient production still remains a challenge and high quality numerical simulation is required in order to understand the physical mechanisms involved. Consequently, a macroscopic numerical model at part scale is actually under development for understanding the relationship between different process and material parameters with the mechanical state of final parts such as distortion and residual stress. Classical finite element method is used to solve the coupled thermo-mechanical problem on the whole domain defined by the workpiece, the baseplate and the support structures. At this scale, powder packing is neglected as well as the hydrodynamics behavior within the melt pool. Homogeneous equivalent heat source is used and imposed until several layers below the current deposited layer. Elastoplastic constitutive material law with temperature dependent parameters has been developed.

1. Introduction

Additive Manufacturing (AM) is becoming an important technology as it provides the production flexibility and part geometry complexity. Among the available processes, the ones treating with metallic alloys receive interest of industrial applications, such as the Selective Laser Melting (SLM), Directed Metal Deposition (DMD) and Electron Beam Melting (EBM). However, due to the difficulty of process control, final parts often suffer from defects like distortion and cracking caused by large thermal gradient. Although many studies have been carried out on this subject, it remains a big challenge for the good process mastery.

Experiments by trial and error approach is very expensive and detailed studied may not been reached. Numerical simulation is thus developed to model the physical phenomena in the process. At the part scale, modeling is more interested in the thermal and mechanical phenomena including stress evolution and final deformation. Macroscopic approach and 3D finite element method are preferred in order to achieve whole part simulation in an affordable computation time. This approach is particularly attractive for industry to design heat extraction by constructing additional support in order to control/master part deformation.

Concerning the management of non-engaged elements during material deposition, two methods inspired from welding modeling are often used: the quiet and inactive element methods [1]. In the former, elements are taken into account while their physical properties are chosen in the way that they have few impact of construction region. In the latter, these elements are not considered at all. Detailed comparison of these methods are given by Michaleris [2]. For the heat source, Goldak model [2] is often used as in welding. Hodge *et al.* [5] used a heat source model based on radiation transfer equation proposed by Gusarov [4]. Another model is based on the Beer-Lambert law taking into account the material absorption, used by Li *et al.* [6] and Chen *et al.* [7], which is suitable for ceramics. Chiumenti *et al.* [3] think that a precise heat source distribution is not mandatory as the right amount of energy introduced in heat affected zone is the most important at a global level. Residual stress investigation was performed by Denlinger *et al.* [8] with a perfect elastoplastic model for Ti-6Al-4V in EBM. By introducing the stress relaxation, good agreement between measurement and simulation in distortion was achieved with appropriate relaxing temperature near to the start of martensitic transformation. Zhang *et al.* [9] used elasto-viscoplastic model for SLM with IN718 alloy. Complex impeller was successfully simulated, while the model was not yet validated by experimental comparison. Bugatti and Semerato *et al.* [10] investigated the inherent method, which introduces the residual plastic strain directly in the simulation. They found better results with inherent strain taken from measurement than that from meso-scale simulation.

In this work, a finite element model for the simulation of additive manufacturing is developed. The thermal and mechanical phenomena are made accessible in reasonable computation time. With appropriate material properties in constitutive model, this model is validated by comparing the part deformation with experiments.

2. Modeling methods

2.1. Process modeling

Macroscale modeling is considered in this work. At this scale the heat source distribution is not modeled in details and an energy deposition model is used. The volumic heat flow is computed considering the laser velocity, laser diameter, hatch space and powder thickness.

$$E_{heat} = \alpha P_{heat} \Delta t_{heat} \tag{1}$$

where Δt_{heat} is the heating time, P_{heat} the heating power and α the powder absorption parameter. This parameter is taken so that the reached nodal temperature is higher than the melting temperature. Δt_{heat} is proportionnal the interaction time with powder, ie the time the laser spends to cross its own diameter.

$$\Delta t_{heat} = \beta \frac{D_{laser}}{V_{laser}} \tag{2}$$

$$P_{heat} = \phi_v V_m \tag{3}$$

$$\phi_v = \frac{P_{laser}}{(D_{laser} e_{powder})} \tag{4}$$

where P_{laser} the laser power, D_{laser}, the laser diameter, e_{powder} the powder thickness, and β the proportionality factor between 0 excluded and 1.

The deposition model is achieved using element activation technique. The initial geometry is meshed so that elements are organized in layers in z direction. To make easier the meshing operation and ensure organization in layers a voxel mesh type is used. Full integrated hexahedral elements are used for their stability.

At time 0, all elements are deactivated then activated layer per layer along the printing simulation. Several other activation strategies are possible notably the so call "*byhatch*" or "*bypath*" strategy, for which element are respectively activated by range or individually following the X or Y global coordinate axis.

To avoid non physical dilatation while heating elements, an intermediate "*powderelement*" with no thermal dilatation is used. This element is active during the heating phase only. Then, when the melting temperature is reached, this element is deactivated and replaced with the permanent melted element.

Surrounding powder is not meshed but simply considered in its insulating action. Equivalent heat exchange parameters are used. This allows to limit the heat exchange with outside on all sides in contact with powder.

The full simulation sequence is decomposed into 4 stages as follows: printing, cooling, cutting from the support plate and spring back. Physical time is used for the simulation. After a new layer activation, the time before the next layer activation includes the heating time, the recoating time and the laser scanning time. This last one is the time the laser will take to scan the entire layer.

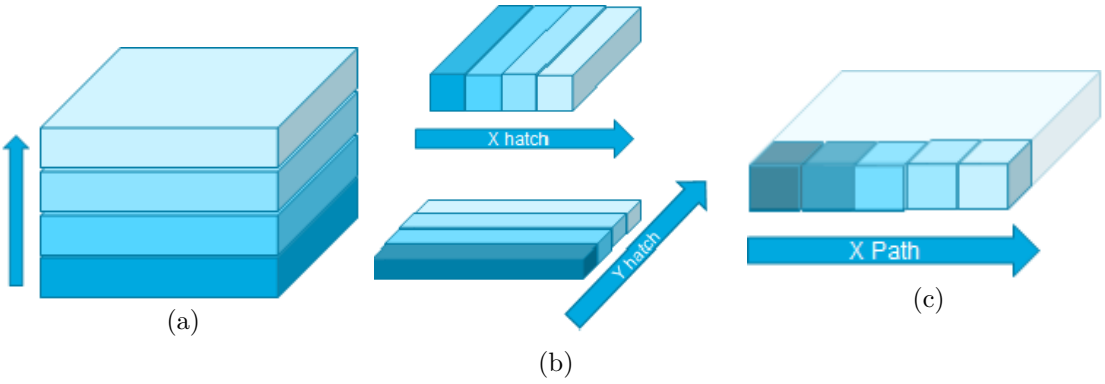

Figure 1: Element activation strategies: (a) by layer in printing direction (Z); (b) by hatch in X or Y direction; (c) by path in X or Y direction.

2.2. Governing equation

In the context of modeling at macro scale, the heat convection, mainly in the melt pool, is not considered. Thus, non-steady heat transfer with only conduction is written as:

$$\rho C_p \frac{\partial T}{\partial t} - \kappa \nabla \cdot (\nabla T) = \dot{q} \tag{5}$$

where T is the temperature, ρ the density, C_p the specific heat, κ the conductivity and $\dot{q}$ the input heat source. Here ρ, C_p and κ are considered as constant.

The initial condition is given by:

$$T(\boldsymbol{x}, 0) = T_0(\boldsymbol{x}) \, \forall \boldsymbol{x} \in \Omega \tag{6}$$

where $T_0(\boldsymbol{x})$ is the imposed initial temperature. For the boundary conditions, both convection and radiation are used:

$$q_c = h_c (T - T_{ext}) \quad \text{on } \Gamma_c \tag{7}$$

$$q_r = \epsilon_r \sigma_r \left(T^4 - T_{ext}^4\right) \quad \text{on } \Gamma_r \tag{8}$$

where $\sigma_r = 5.67 \times 10^{-8}$ W $\cdot$ m^{-2} $\cdot$ K^{-4} is the Stefan-Boltzmann constant, ϵ_r the emissivity, h_c the heat transfer coefficient and T_{ext} the environment temperature. Both convection and radiation are imposed at the top surface in construction. Convection with equivalent h_c is imposed at the lateral surfaces in contact with powder to take into account the heat conduction with powder, in the context of simulation without powder.

For the mechanical modeling, it is based on the equilibrium equation as follows:

$$\rho \frac{\partial \boldsymbol{u}}{\partial t} - \nabla \cdot \underline{\underline{\boldsymbol{\sigma}}} = \rho \boldsymbol{f} \tag{9}$$

where $\boldsymbol{u}$ is the velocity and $\boldsymbol{f}$ the external force. $\underline{\underline{\boldsymbol{\sigma}}}$ is the stress tensor and its relation with deformation is detailed in the next section of material law.

The thermal and mechanical resolution are coupled and solved at each time step with Lagrangian formulation. Acceleration is used for thermal resolution, thus reducing the computation time.

2.3. Material law

The mechanical state is updated by incremental resolution, locally at each Gauss point in each element. Given a total strain increment, the corresponding stress state will be calculated. The total strain rate can be decomposed into elastic, plastic and thermal expansion parts:

$$\dot{\underline{\underline{\boldsymbol{\epsilon}}}} = \dot{\underline{\underline{\boldsymbol{\epsilon}}}}_e + \dot{\underline{\underline{\boldsymbol{\epsilon}}}}_p + \dot{\underline{\underline{\boldsymbol{\epsilon}}}}_{th} \tag{10}$$

This can be split into deviatoric and spherical parts as follows:

$$\begin{cases} \dot{\underline{\underline{\mathbf{e}}}} & = \dot{\underline{\underline{\mathbf{e}}}}_e + \dot{\underline{\underline{\mathbf{e}}}}_p \\ \mathrm{tr}\left(\dot{\underline{\underline{\boldsymbol{\epsilon}}}}\right) & = \mathrm{tr}\left(\dot{\underline{\underline{\boldsymbol{\epsilon}}}}_e\right) + \mathrm{tr}\left(\dot{\underline{\underline{\boldsymbol{\epsilon}}}}_{th}\right) \end{cases} \tag{11}$$

where $\underline{\underline{\mathbf{e}}}$ will be used hereafter for the deviatoric strain. The stress tensor is also split into two parts, the deviatoric and pressure:

$$\begin{cases} \underline{\underline{\boldsymbol{s}}} & = \underline{\underline{\boldsymbol{\sigma}}} + p\underline{\underline{\boldsymbol{I}}} \\ p & = -\frac{1}{3}\mathrm{tr}\left(\underline{\underline{\boldsymbol{\sigma}}}\right) \end{cases} \tag{12}$$

The thermal expansion is related to linear Coefficient of Thermal Expansion (CTE), α, by:

$$\dot{\underline{\underline{\boldsymbol{\epsilon}}}}_{th} = -\alpha \dot{T} \underline{\underline{\boldsymbol{I}}} \tag{13}$$

CTE is temperature dependent and may be different for heating and cooling. It can vary a lot during the phase transformation.

In the case of isotropic material, The Hooke's law is written as:

$$\underline{\underline{\boldsymbol{\sigma}}} = \frac{E}{(1+\nu)} \underline{\underline{\boldsymbol{\epsilon}}}_e + \frac{E\nu}{(1+\nu)(1-2\nu)} \mathrm{tr}\left(\underline{\underline{\boldsymbol{\epsilon}}}_e\right) \underline{\underline{\boldsymbol{I}}} \tag{14}$$

where E is the Young's modulus and ν the Poisson's ratio. Both E and ν are temperature dependent. The former varies a lot with temperature and may be different for heating and cooling, while the latter is almost constant. The elastic strain rate can then be expressed by:

$$\dot{\underline{\underline{\boldsymbol{\epsilon}}}}_e = \frac{1+\nu}{E} \dot{\underline{\underline{\boldsymbol{\sigma}}}} - \frac{\nu}{E} \mathrm{tr}\left(\dot{\underline{\underline{\boldsymbol{\sigma}}}}\right) \underline{\underline{\boldsymbol{I}}} + \frac{d}{dt}\left(\frac{1+\nu}{E}\right) \underline{\underline{\boldsymbol{\sigma}}} - \frac{d}{dt}\left(\frac{\nu}{E}\right) \mathrm{tr}\left(\underline{\underline{\boldsymbol{\sigma}}}\right) \underline{\underline{\boldsymbol{I}}} \tag{15}$$

Splitting the spherical and deviatoric parts results into:

$$\begin{cases} \dot{\underline{\underline{\boldsymbol{\epsilon}}}}_e & = \frac{\dot{\underline{\underline{\boldsymbol{s}}}}}{2\mu} - \frac{1}{2\mu^2}\frac{d\mu}{dt}\underline{\underline{\boldsymbol{s}}} \\ \mathrm{tr}\left(\dot{\underline{\underline{\boldsymbol{\epsilon}}}}_e\right) & = -\frac{\dot{p}}{K} + \frac{1}{K^2}\frac{dK}{dt}p \end{cases} \tag{16}$$

where $K = \frac{E}{3(1-2\nu)}$ is the bulk modulus and $\mu = \frac{E}{2(1+\nu)}$ the shear modulus. This can be rewritten as:

$$\begin{cases} \dot{\underline{\underline{\boldsymbol{s}}}} & = 2\mu\left(\dot{\underline{\underline{\boldsymbol{\epsilon}}}} - \dot{\lambda}\underline{\underline{\boldsymbol{s}}}\right) + \frac{1}{\mu}\frac{d\mu}{dt}\underline{\underline{\boldsymbol{s}}} \\ \dot{p} & = -K\left(\mathrm{tr}\left(\dot{\underline{\underline{\boldsymbol{\epsilon}}}}\right) + \alpha\dot{T}\underline{\underline{\boldsymbol{I}}}\right) + \frac{1}{K}\frac{dK}{dt}p \end{cases} \tag{17}$$

where $\dot{\lambda}$ is the plastic flow rate obtained according to the plastic flow law:

$$\dot{\lambda} = \frac{3\dot{\overline{\epsilon}}_p}{2\overline{\sigma}} \tag{18}$$

with $\dot{\overline{\epsilon}}$ the equivalent strain rate and $\overline{\sigma}$ the equivalent stress.

An elastoplastic Johnson-Cook model is used for the modeling of material behavior:

$$R = \left(A + B\overline{\epsilon}_p^n\right)\left(1 - T_*^m\right) \quad \text{with} \quad T_* = \frac{T - T_r}{T_{melt} - T_r} \tag{19}$$

where A, B, C, m, n are material parameters, T_r the reference temperature and T_{melt} the melting temperature. p is the accumulated plastic strain.

In the local resolution, the flow direction is normal to the yield stress surface in the case of isotropic material. The classical radial return algorithm is used to obtain the material state.

3. Results and discussion

3.1. Ti-6Al-4V cantilever

The cantilever with comb structure is used for the validation of numerical simulation. Its geometry is shown in Figure 4. Its width and height are both 10 mm, with top and bottom length of 100 and 116 mm, respectively. The thickness of the top part is 2 mm. The tooth width of the bottom part is 1 mm with a spacing of 2 mm. The mesh size is set to 1 mm, resulted in 10 layers in total.

The Ti-6Al-4V powder is used for the manufacturing of the cantilever, made in a EOS_M290 machine. The laser power, diameter and scanning speed are 340 W, 80 μm and 1.25 $\mathrm{m \cdot s^{-1}}$, respectively. The hatch space is 80 μm and the recoating time is 9 s. The powder layer thickness is 30 μm. Some constant material properties are detailed in Table 1. The Young's modulus

Table 1: Material properties of Ti-6Al-4V used in modeling.

ρ $\mathrm{kg \cdot m^{-3}}$	κ $\mathrm{W \cdot m^{-1} \cdot K^{-1}}$	C_p $\mathrm{J \cdot kg^{-1} \cdot K^{-1}}$	T_m K	h_c $\mathrm{W \cdot m^{-2} \cdot K^{-1}}$	ϵ_r -
4000	7.1	553	1878	5	0.54

ν -	A MPa	B MPa	n -	m -
0.34	955	350	0.3091	1.12

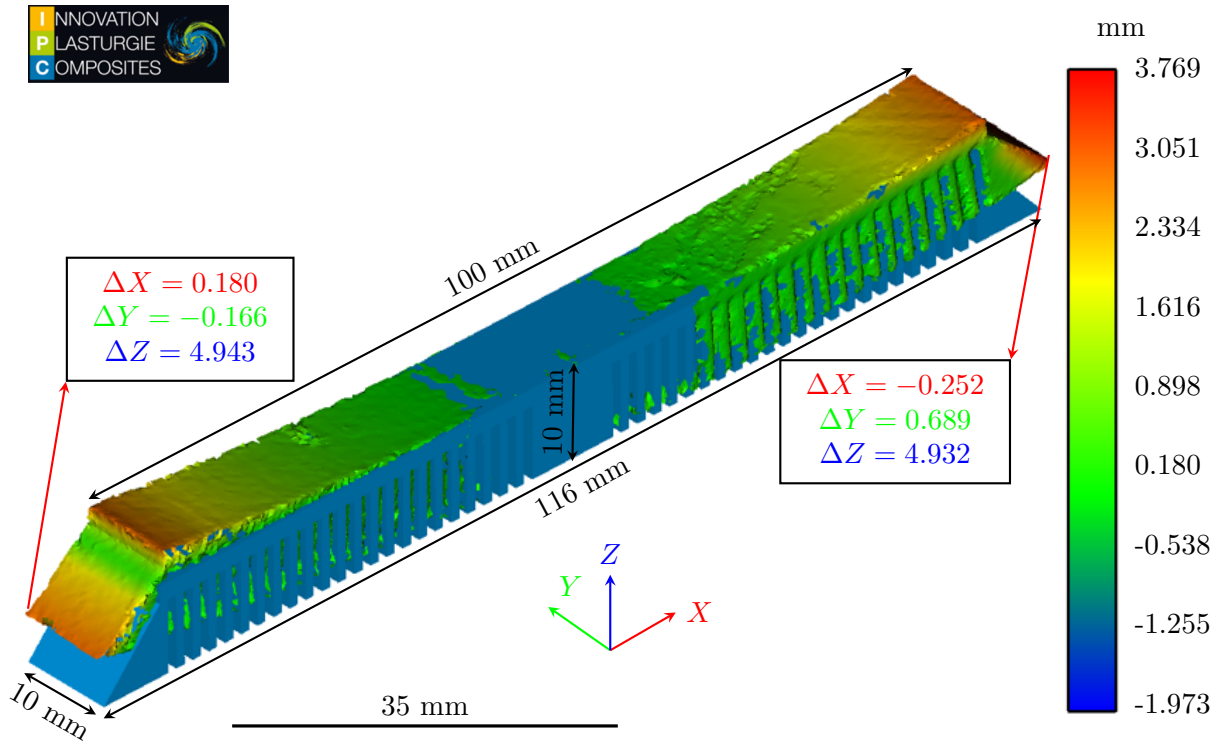

Figure 2: Measured displacement of the cantilever realized by IPC [12].

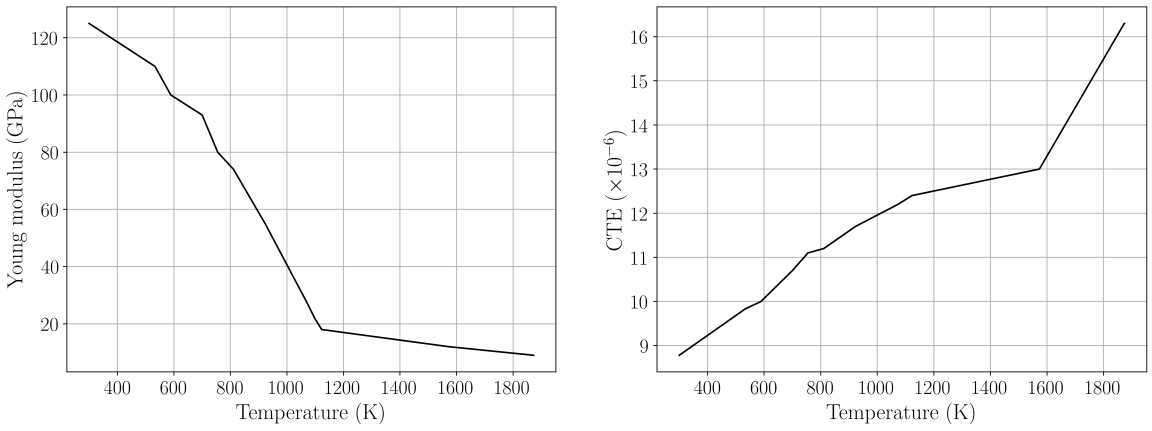

(a) (b)

Figure 3: Properties of Ti-6Al-4V (a) Young's modulus and (b) CTE.

and CTE are measured experimentally. Their temperature dependency is illustrated in Figure 3. The Young's modulus decreases near to 0 when heated to melting point $T_m = 1878$ K. The CTE increases slightly during heating. It is supposed to decrease dramatically to 0 at melting point in order to avoid the thermal expansion in liquid state.

The simulation including 4 stages: the processing, the cooling to near ambient temperature, the cutting from baseplate and the spring back. The final displacement will be compared with experimental measurement, particularly in Z direction. Different acceleration methods are investigated with results detailed in Table 2. The total simulation time is largely decreased by the acceleration of thermal effects. Consequently, the Fast mode takes the least computation time and the Intermediate or Accurate mode takes the most.

Table 2: Comparison of different acceleration methods, executed with 4 Intel 2.8GHz cores.

Acceleration	Fast	Intermediate	Accurate
Time (s)	227	766	755
ΔZ (mm)	6.35	5.05	4.86

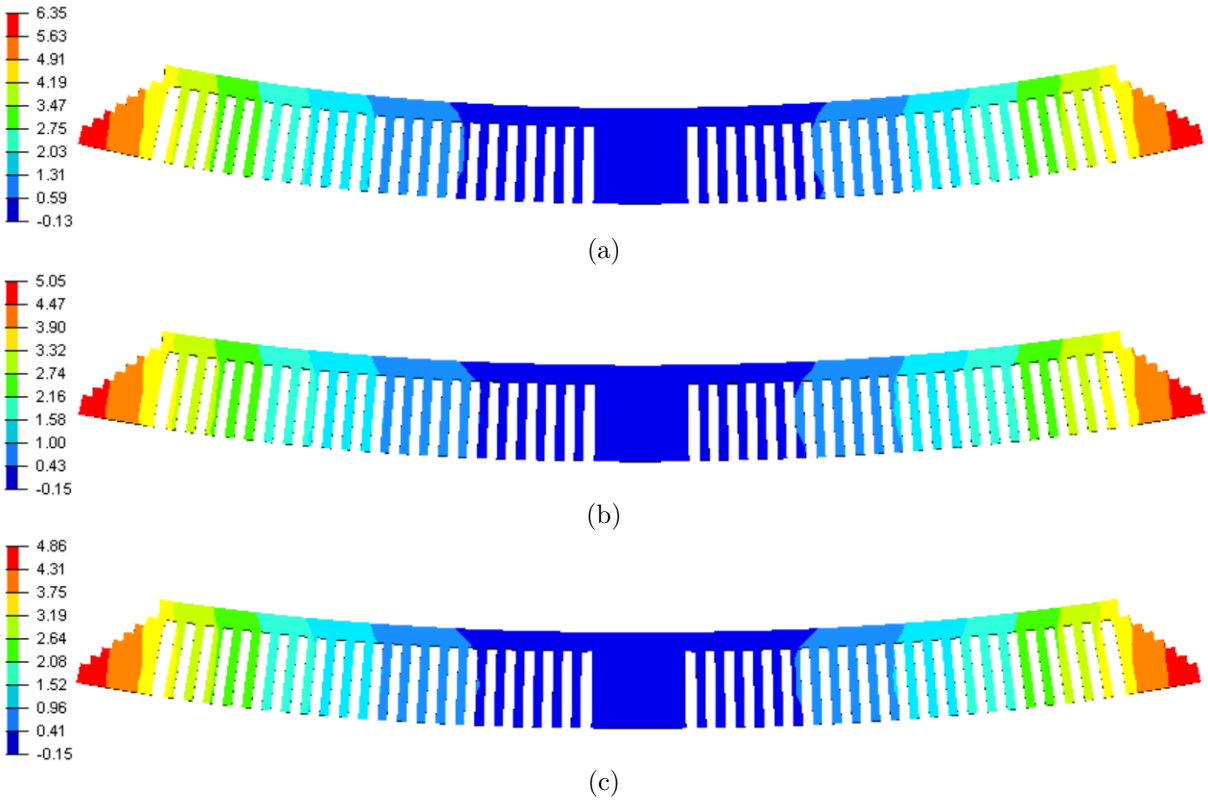

Figure 4: Displacement in Z direction with different simulation acceleration method: (a) Fast; (b) Intermediate; (c) Accurate.

The final displacement ΔZ for different acceleration methods are compared in Figure 4. With high acceleration in Fast mode, $\Delta Z = 6.35$ mm is higher than in other cases, while the

displacement in Intermediate mode is slightly higher than the measurement. With Accurate mode, ΔZ at two sides is very close to experiment, although it takes more time than Fast mode.

The importance of temperature dependent Young's modulus is illustrated by comparing Figure 4(c) with Figure 5, where $E = 125$ GPa. With constant E, the final displacement is largely decreased.

Figure 5: Displacement in Z direction with Accurate mode and constant Young's modulus $E = 125$ GPa.

4. Conclusion

In this work, a macroscopic model for the simulation of additive manufacturing has been developed. By coupling the thermal and mechanical resolution, and considering non-linearities and thermal dependency of both yield stress and elastic modulus, the thermal induced deformation can be reached. An elasto-plastic material law with a temperature dependency is used. The model is validated by experimental comparison of final part deformation after removing from the base plate. The computation time is enhanced by thermal acceleration so that such simulation can be run on a laptop. The future work will be focused on validation with other use cases and more material laws. Phase change will be eventually introduced in our material model to handle more complicated material behavior where christalographic phase transformation is a first order phenomena.

References

[1] Lindgren L-E and Hedblim E, *Commun. Num. Meth. Eng.*, **17(9)**, 647-57
[2] Michaleris P, *Fin. Elem. Anal. Des.*, **86**, 51-60
[3] Chiumenti M, Neiva E, Salsi E, Cervera M, Badia S, Moya J, Chen Z, Lee C and Davies C, *Commun. Num. Meth. Eng.*, **18**, 171-85
[4] Gusarov A V and Kruth J-P, *Int. J. Heat Mass Trans.*, **48(16)**, 3423-34
[5] Hodge N E, Ferencz R M and Solberg J M, *Appl. Surf. Sci.*, **254(4)**, 975-9
[6] Li J F, Li L and Stott F H, *Int. J. Heat Mass Trans.*, **47(6-7)**, 1159-74
[7] Chen Q, Guillemot G, Gandin Ch-A and Bellet M, *Add. Manu.*, **16**, 124-37
[8] Denlinger E R, Heigel J C and Michaleris P, *Proc. Inst. Mech. Eng., B: J. Eng. Manu.*, **229(10)**, 1803-13
[9] Zhang Y, Guillemot G, Bernacki M and Bellet M, *Comp. Meth. Appl. Mech. Eng.*, **331**, 514-35
[10] Bugatti M and Semerato Q, *Add. Manu.*, **23**, 329-46
[11] Carvalho L G, Andrade M S, Plaut R L, Souza F M and Padilha A F, *Mater. Res.*, **16(4)**, 740-4
[12] IPC, Ipc. https://ct-ipc.com. Innovation Plasturgie Composites Center - France.**16(4)**, 740-4